# Energy Circuit Security Region of Energy System (II): Solution and Observation Method

Chenhui Song, *Member, IEEE*, Xinyu Teng, Jun Xiao, *Member*, *IEEE*, Zhengmao Li, Heng Jiao, Qiming Liu

*Abstract*—**The security region is a classic method for power system security analysis, but it is greatly limited when applied to other energy systems and integrated energy systems (IESs). The reason for the above problems is that the physical transmission process and mathematical representation of heterogeneous energy are different, resulting in significant differences in the modeling, solution, and observation of their security regions, as well as a complex solution process. Based on the idea of unified modeling of heterogeneous energy, a unified security region model, called the energy circuit security region (ECSR) is proposed for heterogeneous energy systems and IES for the first time. As a follow-up work on the concept and model of ECSR, this paper focuses on solution and observation methods. Firstly, the concept and model of ECSR are introduced. Secondly, a method for solving and observing the ECSR is proposed, which can not only obtain the complete expression of the security boundary of energy systems in the high-dimensional state space but also observe the region from a full/reduced dimensional perspective. Finally, verification is conducted through typical electrical power systems (EPSs), natural gas systems (NGSs), and IESs. The results show that the proposed method is unified for both single heterogeneous energy systems and IESs. Compared with existing methods, it can directly analyze the security of any operating point in high-dimensional state space, greatly improving efficiency while ensuring accuracy, and maintaining the advantages of region methods in security analysis.**

*Index Terms*—**integrated energy system; electrical power system; natural gas system; energy circuit security region; solution; observation**

## I. INTRODUCTION

The security region originates from the electrical power system (EPS), which refers to the set of all operating point

Chenhui Song is with the State Key Laboratory of Disaster Prevention & Reduction for Power Grid, Changsha University of Science and Technology, Changsha 410114, China, and also with the State Key Laboratory of Intelligent Power Distribution Equipment and System, Tianjin University, Tianjin 300072, China, (e-mail: songchenhui66399@163.com).

Xinyu Teng is with the State Key Laboratory of Disaster Prevention & Reduction for Power Grid, Changsha University of Science and Technology, Changsha 410114, China, (e-mail: 19882483445@163.com).

Jun Xiao and Qiming Liu are with the State Key Laboratory of Intelligent Power Distribution Equipment and System, Tianjin University, Tianjin 300072, China, (e-mail: xiaojun@tju.edu.cn; 18852281668@163.com).

Zhengmao Li is with the School of Electrical Engineering, Aalto University, 02150 Espoo, Finland, (e-mail: zhengmao.li@aalto.fi).

Heng Jiao is with the School of Information and Electrical Engineering, Hebei University of Engineering, Handan 056038, China, (e-mail: jiaoheng@tju.edu.cn).

that can ensure that all components of the system meet certain secure criteria during operation [1]. Since its first proposal in 1975, the security region method has gradually established relatively complete theoretical criteria in terms of concepts [2-4], models [2-4], and property mechanisms [4-6]. Compared with the "point by point method", the region method has the following advantages in security analysis [4]:

(1) The security region pre-completes processes such as power flow calculation offline. During online analysis, by comparing the relative positions of the operating point and the region, the security of the current state can be accurately evaluated, greatly improving the efficiency of online security analysis of the operating point.

(2) The security region describes the global information of the system in the state space. After obtaining the overall security measurement of the system, it is easy to achieve situational awareness and proactive prevention, which helps to develop new transformation planning methods [7].

In addition to EPS, the research on the security region of other energy systems like natural gas systems (NGSs) has also gradually received attention [8-15], especially the integrated energy system (IES) with heterogeneous energy coupling. Due to the cascading effect of fault disturbance that existed in IES, the security region of IES (IES-SR) has become a current research hotspot [12-15]. However, when IES-SR is applied, there still exists the following problem:

First of all, though the security region calculation could be completed offline, the computational complexity of solving and observing the security region in high-dimensional space is very high. This is because of the complex multi-energy flow calculation process and the high dimension of operating points. However, if we use dimension reduction methods to alleviate the computational burdens, it will result in a significant loss of information, which makes it difficult to utilize the global information of IES-SR.

Regarding the above issues, the solution and observation of IES-SR are gaining increasing research interest from both academia and industry [15-18]. Ref. [15] proposes a solution method for IES-SR based on vertex algorithm and spatial projection. Ref. [16] verified the correspondence between IES-SR and the conventional stable equilibrium manifold of the gradient dynamics system, which helps calculate IES-SR through theoretical and numerical methods. Based on [16], the study in [17] proposed an IES-SR solution method for fast-slow dynamic systems. Ref. [18] proposed an IES-SR solution method based on polyhedral equivalent projection and flexible

constraint relaxation. However, the solution and observation methods are still in their early stages and have the following shortcomings:

(1) A general observation and observation method for the security regions of heterogeneous energy systems and IES has not been formed yet.

(2) The improvement of the solution is mainly based on different algorithms, which do not involve the improvement of the models of security regions. This leads to the limited effect of improving the solution efficiency.

(3) Based on the reduced dimension, without the complete full-dimension expression, the application of security region in high-dimensional space has great limitations.

The unified modeling of heterogeneous energy provides a solution to the above shortcomings [19-26], the method aims to establish a formal unified mathematical model, which considers the differences in transmission characteristics of heterogeneous energy systems but the similarities in their network features. Among them, Ref. [19-21] draw on the modeling process of EPS from "electromagnetic field" to "circuit" and propose an energy circuit model for IES analysis, which has the advantages of strong interpretability and easy scalability [19, 21]. These advantages make the energy circuit model suitable for standardized modeling of the security regions for heterogeneous energy systems. It is expected to improve the offline solving efficiency of regions at the model level.

This series of papers proposes the energy circuit security region (ECSR) for energy systems. As the second paper in the series, this paper focuses on the solution and observation of the ECSR based on previous work on ECSR modeling. The rest of this paper is arranged as follows. The first section briefly

reviews the concept and model of ECSR. In the second section, a generalized ECSR solution method applicable to different energy systems is proposed to address the difficulties in solving security regions. The third section presents a generalized observation method for ECSR. The fourth section continues the modeling results of the case study of the first paper, which solves and observes the ECSRs of EPS, natural gas system (NGS), and IES. Compared with existing methods, this paper improves the efficiency of solving security boundary points at the model level; the complete full-dimensional security boundary analytical expressions for large-scale examples of different energy systems are obtained for the first time, which can directly achieve security analysis for any operating point in high-dimensional state space.

## II. Concept and Model of ECSR

### A. Energy circuit security region (ECSR) model

ECSR refers to the security region model established for the energy system based on the energy circuit. The modeling of ECSR for heterogeneous energy systems and IESs is universal: network equations are used to describe the energy balance relationship of the network, while other constraints only need to consider the secure operating conditions of the components in the system.

The article [27] modeled the ECSR of an electric power system (EPS-ECSR), the ECSR of a natural gas system (NGS-ECSR), and the ECSR of IES (IES-ECSR), the results are shown in Table I. It can be seen the models of ECSRs have good uniformity and their forms are also very concise.

TABLE I
ECSR MODELS OF EPS, NGS, AND IES

| EPS-ECSR | NGS-ECSR | IES-ECSR |
|---|---|---|
| $\Omega_{\text{EPS-ECSR}} = \{W_s \mid h(W_s) = 0, g(W_s) \le 0\}$ <br><br> $s.t. \begin{cases} Y_e U_n = I_n \quad \text{balance constraint} \\ \begin{rcases} I_n^{\min} \le I_n \le I_n^{\max} \\ U_n^{\min} \le U_n \le U_n^{\max} \\ I_b \le I_b^{\max} \\ K_e^{\min} \le K_e \le K_e^{\max} \end{rcases} \text{security constraint} \end{cases}$ | $\Omega_{\text{NGS-ECSR}} = \{W_s \mid h(W_s) = 0, g(W_s) \le 0\}$ <br><br> $s.t. \begin{cases} Y_g p_n = G_n \quad \text{balance constraint} \\ \begin{rcases} G_n^{\min} \le G_n \le G_n^{\max} \\ p_n^{\min} \le p_n \le p_n^{\max} \\ -A_{g,L}^{-1} G_n \le G_b^{\max} \\ K_g^{\min} \le K_g \le K_g^{\max} \end{rcases} \text{security constraint} \end{cases}$ | $\Omega_{\text{IES-ECSR}} = \{W_s \mid h(W_s) = 0, g(W_s) \le 0\}$ <br><br> $s.t. \begin{cases} Y_{\text{IES}} P_n = F_n \quad \text{balance constraint} \\ \begin{rcases} P_n^{\min} \le P_n \le P_n^{\max} \\ F_n^{\min} \le F_n \le F_n^{\max} \\ F_b \le F_b^{\max} \\ K^{\min} \le K \le K^{\max} \end{rcases} \text{security constraint} \\ \begin{rcases} g_m = f(h_m) \\ g_m \subseteq F_n, h_m \subseteq F_n \end{rcases} \text{coupling constraint} \end{cases}$ |

### B. Security boundary model

The security boundary is the boundary between the secure and insecure subspaces of operating points in the state space, it is the key to solving the security region. The security boundary is defined as the set of all critical operating points in the security region, denoted as $\partial\Omega_{\text{SR}}$. The definition of a critical operating point is as follows: For a secure operating point, is there at least one load that may lead the system to an insecure state when its power/flow increases or decreases; If the load exists, the system is critically secure, and the original operating point is the critically secure operating point, abbreviated as the critical

point, denoted as $W_b$.

The critical security caused by an increase in power/flow rate is defined as positive criticality, while the critical security caused by a decrease in power/flow rate is defined as negative criticality. According to the positive and negative criticality, the security boundary can be divided into the upper boundary and the lower boundary: all critical points with positive criticality constitute the upper boundary, denoted as $\partial\Omega_{\text{SR}}^+$; all critical points with negative criticality constitute the lower boundary, denoted as $\partial\Omega_{\text{SR}}^-$. Because the security boundary is composed of critical points, it is also customary to refer to critical points

as boundary points.

The model of security boundary is shown as equation (4), its meaning is as follows: $\partial\Omega_{SR}$ is a universal symbol for the security boundaries of different systems, and $x_i$ represents the element of the operating point. $W_b \in \boldsymbol{\Omega}_{SR}$ indicates that the operating point $W_b$ is located in the security region and it is a security point. A new working point $W^*$ will be formed after an element of $W_b$ increases with $\varepsilon$. If $\varepsilon^*>0$, then $W_b$ has positive criticality and is located at the upper boundary, it is an upper boundary point. If $\varepsilon^*<0$, then $W_b$ has negative criticality and is located at the lower boundary, it is a lower boundary point.

$$\partial\boldsymbol{\Omega}_{SR}=\left\{W_b \left| \begin{array}{l} [x_1,...,x_i,...,x_j...,x_n]=W_b \in \boldsymbol{\Omega}_{SR} \\ W^*=[x_1^*,...,x_i^*,...,x_j^*,...,x_n^*] \\ x_i^*=x_i+\varepsilon^* \\ x_j^*=x_j(j \neq i) \\ \forall \varepsilon^* \neq 0, \ \exists i=1,2,\cdots,n, \ W^* \notin \boldsymbol{\Omega}_{SR} \end{array} \right. \right\} \quad (1)$$

It should be noted the security region is formed by the security boundary cutting the state space, so the complete boundary generally contains some state space boundaries.

## III. SOLUTION METHOD OF ECSR

### A. Challenges and solutions

Security region is usually a hyper polyhedron in high-dimensional state space, there exist two challenges in solving it.

**Challenge 1**: the efficiency of solving high-dimensional security regions is low. When solving the traditional boundary points, it is necessary to verify the security of operating points through multi-energy flow calculation [28]; With the increase of security region dimension, the number of operating points to be verified will increase exponentially. If the multi-energy flow calculation is still based on the inherent energy flow equations of heterogeneous energy systems, it will take a lot of time.

**Challenge 2:** it is difficult to solve the complete boundary expressions of security regions in high-dimensional space. It is because, in the high-dimensional space, it is difficult to directly observe the security region in the form of a super polyhedron, which means it is impossible to directly observe the boundary of the security region where there is a large curvature change. The challenge of finding the piecewise point when fitting the security boundary brings a big challenge in solving high dimensional boundaries.

The solutions to the above challenges are as follows:

(1) For **Challenge 1**, when solving the ECSR in this paper, the traditional nonlinear energy flow equation [20-21] is replaced by the network equation during the multi-energy flow calculation, which can avoid the iterative process of solving the nonlinear equation to a certain extent and greatly save the calculation time.

(2) For **Challenge 2**, a piecewise point solution method by calculating the distance from the boundary points to the hyperplane is proposed: in each piecewise fitting, the boundary point with the largest distance from all boundary points to the current hyperplane is the piecewise point. The boundary of

curvature change of security position can be obtained without observation through the method.

### B. Solution method

For solving the ECSR of heterogeneous energy systems and IES, this paper proposes a general method: first, solve the network equation to obtain the complete state of the operating point; Second, the boundary points are solved through criticality check; finally, the security boundary expressions are obtained by fitting the boundary points.

#### 1) Solution of heterogeneous energy network equations

The solution of the network equation of EPS is relatively mature and will not be repeated. The following describes the network equation solution method of NGS [22,28], as well as the processing method of coupling element constraints between heterogeneous energy systems.

a) Network equation solution method

The network equation describes the equilibrium relationship between nodal pressure and the flow of NGS. Since the node pressure and injection flow can be obtained directly during actual operation, the network equation of NGS can be obtained. The specific process is as follows.

First, by analogy with EPS, the nodes of NGS are divided into constant pressure nodes and constant flow nodes according to the energy flow calculation of the NGS, i.e. the known state quantity and the state quantity to be calculated during the hydraulic calculation, as shown in Table II.

TABLE II
NODE CLASSIFICATION IN SOLVING NETWORK EQUATION OF NGS

| Node | Type | Known state | State to be calculated |
|---|---|---|---|
| Source | constant pressure node | node pressure | node flow |
| Load | constant flow-node | node flow | node pressure |
| Others | constant flow-node | node flow (0) | node pressure |

Second, according to the node type, rearrange the network equation shown in formula (14) of Ref. [28] by line, as follows:

$$\begin{bmatrix} Y_{G,pp} & Y_{G,pg} \\ Y_{G,gp} & Y_{G,gg} \end{bmatrix} \begin{bmatrix} p_{n,p} \\ p_{n,g} \end{bmatrix} = \begin{bmatrix} G_{n,p} \\ G_{n,g} \end{bmatrix} \quad (2)$$

where, $p_{n,p}$ and $G_{n,p}$ are vectors composed of node pressure and injection flow of constant pressure node, $p_{n,g}$ and $G_{n,g}$ are vectors composed of node pressure and injection flow of constant flow node, $Y_{g,pp}$, $Y_{g,pg}$, $Y_{g,gp}$ and $Y_{g,gg}$ are corresponding matrix blocks after $Y_G$ rearrangement.

Finally, equation (2) can be used to solve $G_{n,p}$, and $p_{n,g}$ of the nodes, as shown in equations (3) and (4):

$$G_{n,p}=Y_{G,pp}p_{n,p}+Y_{G,pg}p_{n,g} \quad (3)$$

$$p_{n,g}=Y_{G,pg}^{-1}(G_{n,g}-Y_{G,gp}p_{n,p}) \quad (4)$$

b) Processing method of coupling unit constraint

Taking the two types of typical coupling units shown in Figure 1 of [28], namely, electric-driven compressors and gas generators as examples, the coupling unit constraint processing method of IES is introduced.

First, based on the energy flow relationship, the nodes of the coupling units in the heterogeneous energy system are classified, as shown in Table III:

TABLE III
NODE CLASSIFICATION OF COUPLING UNIT

| Coupling unit | In EPS | In NGS |
|---|---|---|
| Electric driven compressor | PQ node | constant flow-node |
| Gas generator | PV node | constant flow-node |

Secondly, according to the node classification of the coupling unit in NGS, it is assigned values based on the state variables corresponding to the operating point, the network equation of NGS is solved to obtain the complete state variables of the NGS at that operating point.

Thirdly, based on the complete state variables of NGS and the coupling element constraint equation in equation (18) of [28], the required state variables of coupling units for solving the network equation of EPS are calculated, and the parameter transfer between heterogeneous energy systems is achieved.

Finally, after obtaining the required state variables for solving the network equation of EPS, the network equation is solved to obtain the complete state variables of EPS corresponding to the operating points.

*2) Solution of security boundary points*

For solving security boundary points, this section proposes a universal solution method based on binary division: iteratively modifying the operating point to the boundary point. Using the binary method for solving can ensure convergence from the initial point to the boundary point, the number of iterations during correction can be reduced meanwhile, which improves the efficiency.

This method mainly includes two processes: security verification and criticality verification. Taking the upper boundary point solution as an example, this process will be briefly described. The overall idea is as follows: when solving boundary points, any element of the selected operating point is modified, and the remaining elements are sampled with equal intervals.

For the *k*-th operating point, the processes of security verification and criticality verification are as follows.

*(1) Security verification*

Firstly, according to the known state variables corresponding to the operating point, the complete state variables are solved by solving the network equations.

Secondly, based on equations (17)~(19) in Ref. [28], check whether all the state variables corresponding to the operating point meet the security constraints: if so, the point is located in the security region, and its criticality needs to be checked to determine whether the point is close enough to the boundary; if not, the point is located outside the security region and above the upper boundary, so it needs to be modified in the negative direction, that is, the selected element in the point is reduced by the correction step, then the security verification of the corrected operating point is carried out again.

*(2) Criticality verification*

The criticality of an operating point is verified by judging whether the correction step meets the convergence condition. If the criticality is satisfied, the operating point meets the criticality and is close enough to the boundary, the *k*-th boundary point is obtained, next operating point is continued to

be modified. If the criticality is not satisfied, although the operating point is located in the region, the point is far from the upper boundary, it needs to be modified in the positive direction further, that is, the selected element of the point is added with the correction step, then the security of the modified point is verified again.

It should be noted that during the modification process of each operating point, if the security of the point changes compared with the last modification, bisection for the correction step should be performed until the correction step is less than the convergence accuracy and the boundary point is obtained. Then, the initial value of the correction step is reassigned to solve the next boundary point. The binary division ensures the fast convergence of the modification process.

*3) Security boundary fitting*

Full-dimensional security boundary points can reflect the global characteristics of the security region. However, their discrete nature makes direct application challenging, while obtaining complete boundary expressions in high-dimensional spaces remains intractable (i.e., **Challenge 2** in Section 3.1). To address this, we propose a segmented solution approach based on calculating the distance from boundary points to hyperplanes. This method automatically identifies curvature change points on security boundaries without requiring prior observation, enabling the characterization of energy system security boundaries through a set of hyperplanes. This achieves piecewise fitting of full-dimensional security boundary expressions.

Further, the proposed security boundary fitting method exhibits universality: it can derive security boundary expressions for arbitrary single-energy systems and IES of any dimensionality. This capability comprehensively delineates the secure operational ranges of energy systems, facilitating practical implementation in online analysis. The detailed procedure is as follows.

a) Setting the distance error threshold $D^{\max}$.

The $D^{\max}$ defines the maximum allowable distance between all boundary points and the fitted hyperplanes. It quantifies the precision of hyperplane fitting and serves as the termination criterion for the piecewise fitting process.

b) Constructing the initial hyperplane

First, to enhance computational efficiency while maintaining accuracy, the number of fitting iterations should be minimized. For the initial hyperplane in the first fitting iteration, boundary points that maximize the coverage of the region are selected to construct the hyperplane. The equation of the initial hyperplane is expressed as:

$$H^0 : \sum_{i=1}^{N} a_i^0 \omega_i + b^0 = 0 \tag{5}$$

where, $H^0$ denotes the initial hyperplane equation, $a_i^0$ and $b^0$ represent the fitting coefficients of $H^0$, these coefficients can be calculated from the selected boundary points during the fitting process. The variable $\omega_i$ in the $H^0$ corresponds to the elements of operating points, while $N$ indicates the security region dimension. $N$ simultaneously determines both the number of elements in operating points and the variable quantity in the

hyperplane equation.

Second, the distance from each boundary point to $\boldsymbol{H}^0$ is computed. For a boundary point $\boldsymbol{W}_\mathrm{b}=[x_1,\ldots,x_i,\ldots x_N]$, its distance to $\boldsymbol{H}^0$ is expressed in equation (6):

$$D_{W_\mathrm{b}\rightarrow H^0} = \frac{|\sum_{i=1}^{N} a_i^0 x_i + b^0|}{\|a_i^0\|_2} \quad (6)$$

where, $\boldsymbol{a}_i^0$ denotes the vector formed by $a_i^0$, $\|\boldsymbol{a}_i^0\|_2$ represents its Euclidean norm.

Finally, the boundary point exhibiting the maximum distance $\boldsymbol{W}_\mathrm{b}^{(0)}$ to $\boldsymbol{H}^0$ is identified from all candidate points. The fitting precision of $\boldsymbol{H}^0$ is then assessed against the criterion $D_{W_\mathrm{b}\rightarrow H^0}^{\max} \leq D^{\max}$:

The boundary point $\boldsymbol{W}_\mathrm{b}^{(0)}$ corresponding to the maximum distance $D_{W_\mathrm{b}\rightarrow H^0}^{\max}$ from the point to $\boldsymbol{H}^0$ is identified through systematic evaluation. The hyperplane fitting accuracy is verified against the criterion: if $D_{W_\mathrm{b}\rightarrow H^0}^{\max} \leq D^{\max}$ is satisfied, $\boldsymbol{H}^0$ is the definitive security boundary expression; if unsatisfied, an initial segmented fitting is implemented with the partition point $\boldsymbol{W}_\mathrm{b}^{(0)}$. This process regroups the original boundary points selected for $\boldsymbol{H}^0$ construction.

c) Piecewise Linear Fitting

The $k$-th segmented fitting iteration proceeds as follows. First, the selected boundary points are grouped and fitted into hyperplanes following equation (5), yielding $M$ hyperplane equations. Second, the orthogonal distances from boundary point $\boldsymbol{W}_\mathrm{b}$ to each hyperplane are computed using equation (6), with the minimum distance selected as defined in equation (7):

$$D_{W_\mathrm{b}\rightarrow H^k} = \min(D_{W_\mathrm{b}\rightarrow H_j^k}) , j = 1,\ldots,M \quad (7)$$

where, $D_{W_\mathrm{b}\rightarrow H^k}$ is the minimum distance from $\boldsymbol{W}_\mathrm{b}$ to all hyperplanes, $D_{W_\mathrm{b}\rightarrow H_j^k}$ is the distance from $\boldsymbol{W}_\mathrm{b}$ to $\boldsymbol{H}_j^k$.

Finally, for every boundary point, calculate its $D_{W_\mathrm{b}\rightarrow H^k}$, take its maximum value, denoted as $D_{W_\mathrm{b}\rightarrow H^k}^{\max}$, with its corresponding boundary point labeled as $\boldsymbol{W}_\mathrm{b}^{(k)}$. The fitting accuracy of the hyperplane obtained in the $k$-th segmented fitting iteration is then evaluated: if $D_{W_\mathrm{b}\rightarrow H^k}^{\max} \leq D^{\max}$, the accuracy requirement is satisfied, the current hyperplane serves as a final security boundary; otherwise, the fitting precision is deemed insufficient, requiring the boundary points selected during the $k$-th iteration to be regrouped using $\boldsymbol{W}_\mathrm{b}^{(k)}$ as the segmentation point, followed by a subsequent $(k+1)$-th piecewise linear fitting iteration.

## IV. OBSERVATION METHOD OF ECSR

### A. *Direct observation based on dimensionality reduction*

The ECSR is typically a high-dimensional polyhedron in the state space. Its two-dimensional (2D) or three-dimensional (3D) cross-sectional views can be directly visualized through dimensionality reduction-based observation. Taking 2D cross-sectional observation as an example, the procedure is outlined below.

(1) Select observation variables. Choose two elements $x_i$ and $x_j$ from the operating point as the observation variables, and fix the remaining elements as constants.

(2) Calculate observation variables. Perform equidistant sampling on $x_i$, and iteratively adjust $x_j$ using the method in section 3.2.2 to calculate the upper and lower boundary points of the cross-section of ECSR in the 2D space.

(3) Draw Cross-sectional Views. Fit the upper and lower boundary points of the security region cross-section, and plot the results on the $x_i$-o-$x_j$ plane to obtain the upper and lower boundary views of the cross-section. The closed area formed by these two boundaries intersecting the $x_i$ and $x_j$ state space boundaries constitutes the two-dimensional view of the region.

For 3D views, simply add one more observed variable during the process of "Selecting observed variables" and perform equidistant sampling on it.

Through dimensionality reduction observation, the 2D/3D cross-sectional views of ECSR can be directly observed. However, dimensionality reduction methods can only visualize the local boundaries of a region in low-dimensional space and cannot capture its global information in high-dimensional space. Additionally, the 2D/3D cross-sectional views of the ECSR may vary significantly depending on the observation perspective. Therefore, when observing the region using dimensionality reduction methods, it is generally necessary to combine multiple related cross-sectional information.

### B. *Full-dimensional indirect observation method*

Full-dimensional observation enables comprehensive visualization of security regions by characterizing their morphological features in high-dimensional spaces [7,30]. However, direct visualization of high-dimensional geometries in low-dimensional planes remains challenging, thus requiring indirect observation approaches.

This paper adopts a full-dimensional indirect observation method for ECSR. The methodology is structured as follows: as demonstrated in Section 2.2.3, ECSR boundaries comprise a set of hyperplanes that collectively form a high-dimensional hyper-polyhedron, the security margin, defined as the distance from the hyper-polyhedron's centroid to each hyperplane, quantifies the degree of concavity and convexity in the security region, the margin can be used for full-dimensional indirect observation.

The procedure of the method involves two main steps:

(1) Calculation of minimum security margins. Following the definition of minimum security margins for distribution network security boundaries, the minimum distance from the origin of ECSR to each hyperplane $\boldsymbol{H}_i$ is computed through equation (5), represented as $\boldsymbol{D}_i$.

(2) Visualization via Radar Chart. A radar chart (Fig. 1) is constructed with the origin as the center and the minimum margins $\boldsymbol{D}_i$ as radial data points. This visualization establishes a one-to-one correspondence between the radar chart's

boundary profile and the ECSR geometry, enabling intuitive identification of concave or convex regions in the ECSR.
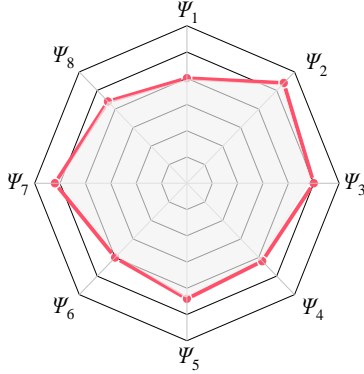


Fig. 1. Diagram of full-dimensional indirect observation of ECSR

## V. CASE STUDY

The IEEE 14-node EPS, Belgian 9-node NGS, and 23-node IES from reference [28] are adopted for verification. Ref.[28] derived and established ECSR models for these three cases, with results provided in Appendix B. Further solving and observation of the ECSR models are conducted: the solving results include security boundary points and boundary equations, while the observation results include 2D/3D/full-dimensional views of the ECSRs.

The experimental environment is configured as follows: an Intel(R) Core(TM) i5-2450M CPU @ 2.50GHz processor, 4GB memory, and the IntelliJ IDEA simulation platform.

### A. Solution and observation of EPS-ECSR

#### 1) Solution of EPS-ECSR

The parameter settings for boundary point calculation are as follows: in the state space, loads of nodes $N_{e1} \sim N_{e13}$ are sampled at equal intervals with a sampling step size of 5MVA. The load of $N_{e14}$, i.e. $S_{l,e14}$ is modified, and the convergence accuracy of modify step size is 0.01MVA.

The EPS-ECSR modeling results are detailed in Sections 5.2.1 and 5.3.1 of Ref. [28] or Appendix B of this paper. The specific solution procedure is described below.

First, according to section 3.2.2 "(1) Security verification", perform verification on the operating point as follows.

The operating point to be validated is substituted into equation (20) Ref. [28] along with given state parameters, and multi-energy flow calculation is performed using network equations. Since the network equations constitute a system of linear equations where the coefficient matrix and augmented matrix share equal rank, there exists a unique solution that enables the complete determination of state variables at the operating point. If all state variables satisfy the security constraints specified in equation (20), the operating point is considered secure; otherwise, it is insecure.

Second, the security boundary points are identified following "(2) Criticality validation" of Section 2.2.2. The initial operating point is adjusted towards boundary points based on security analysis results. Fig. 2 demonstrates this iterative refinement process using boundary point $W_{b,1}$ (20, 85, 40, 0, 0,

25, 0, 5, 5, 0, 19.25) as an exemplar of upper boundary point determination. The specific implementation procedure comprises the following steps.
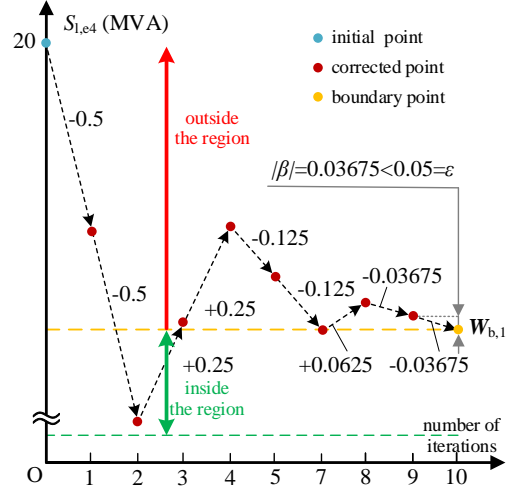


Fig. 2. Iterative correction process of boundary point $W_{b,1}$

(1) Initialize the upper limit of $S_{l,e14}$ at the initial operating point as 20MVA, set the initial correction step size $\beta$ to 0.5MVA (where "+" and "-" denote positive and negative adjustment directions), and define the convergence tolerance $\varepsilon$ as 0.05MVA.

(2) Validate the security of the corrected operating point and adjust $S_{l,e14}$ through positive or negative corrections based on validation results. Each reversal of correction direction triggers an update of the step size as $\beta=\frac{1}{2}\beta$.

(3) After 10 iterative corrections, the operating point satisfies security requirements with $|\beta|=0.03675MVA<0.05MVA$, achieving the predefined convergence tolerance, and the boundary point $W_{b,1}$ is obtained.

Finally, 19716 upper boundary points and 4255 lower boundary points are obtained, as shown in Table IV.

TABLE IV
UPPER AND LOWER BOUNDARY POINTS IN EPS-ECSR OF IEEE 14-BUS SYSTEM

| | | $(S_{l,e2}, S_{l,e3}, S_{l,e4}, S_{l,e5}, S_{l,e6}, S_{l,e9}, S_{l,e10}, S_{l,e11}, S_{l,e12}, S_{l,e13}, S_{l,e14})$ |
|---|---|---|
| Upper boundary point | $W_{b,1}$ | (20, 85, 40, 0, 0, 25, 0, 5, 5, 0, 19.25) |
| | $W_{b,2}$ | (20, 85, 40, 0, 0, 25, 0, 5, 5, 5, 17.18) |
| | $W_{b,3}$ | (20, 85, 40, 0, 0, 25, 0, 5, 5, 10, 14.06) |
| | $W_{b,4}$ | (20, 85, 40, 0, 0, 25, 0, 5, 5, 15, 11.22) |
| | $W_{b,5}$ | (20, 85, 40, 0, 0, 25, 0, 5, 10, 0, 17.47) |
| | … | … |
| | $W_{b,19715}$ | (30, 100, 45, 10, 15, 25, 0, 5, 0, 0, 13.74) |
| | $W_{b,19716}$ | (30, 100, 45, 10, 15, 25, 0, 5, 0, 5, 11.88) |
| Lower boundary point | $W_{b,1}$ | (30, 100, 45, 10, 15, 25, 0, 5, 0, 5, 10.00) |
| | $W_{b,2}$ | (30, 100, 45, 10, 15, 25, 0, 5, 0, 0, 11.24) |
| | $W_{b,3}$ | (30, 100, 45, 10, 15, 25, 0, 0, 5, 5, 10.87) |
| | $W_{b,4}$ | (30, 100, 45, 10, 15, 25, 0, 0, 5, 0, 11.73) |
| | $W_{b,5}$ | (30, 100, 45, 10, 15, 25, 0, 0, 0, 5, 11.51) |
| | … | … |
| | $W_{b,4254}$ | (20, 100, 45, 0, 0, 25, 0, 0, 5, 15, 11.89) |
| | $W_{b,4255}$ | (20, 100, 45, 0, 0, 25, 0, 0, 5, 10, 13.06) |

Using boundary points to fit the security boundary and setting an error threshold of 0.1, 83 upper boundary hyperplanes and 46 lower boundary hyperplanes are obtained, as shown in Table V. The region enclosed by the upper and lower boundary-

cutting state space is EPS-ECSR.

TABLE V
EXPRESSION OF SECURITY BOUNDARY OF EPS-ECSR OF IEEE 14-BUS SYSTEM

| | Hyperplane | Expression |
|---|---|---|
| Upper boundary | $\psi_1^{upper}$ | $21746S_{1,e2}+9523S_{1,e3}-18400S_{1,e4}+68235S_{1,e5}+22348S_{1,e6}+45135S_{1,e9}-31692S_{1,e10}+11582S_{1,e11}+21243S_{1,e12}-65255S_{1,e13}-12487S_{1,e14}-52710=0$ |
| | $\psi_2^{upper}$ | $15514S_{1,e2}+8750S_{1,e3}+10023S_{1,e4}-55351S_{1,e5}-65252S_{1,e6}+54101S_{1,e9}+10512S_{1,e10}-25135S_{1,e11}+9085S_{1,e12}-10552S_{1,e13}-11443S_{1,e14}+45801=0$ |
| | $\psi_3^{upper}$ | $19545S_{1,e2}+9228S_{1,e3}-10441S_{1,e4}+17042S_{1,e5}-52551S_{1,e6}+15412S_{1,e9}-11488S_{1,e10}-15223S_{1,e11}+20841S_{1,e12}+28331S_{1,e13}-33571S_{1,e14}+39112=0$ |
| | … | |
| | $\psi_{82}^{upper}$ | $9280S_{1,e2}+17525S_{1,e3}+11480S_{1,e4}+22514S_{1,e5}-60368S_{1,e6}-32135S_{1,e9}+20126S_{1,e10}+10228S_{1,e11}-4034S_{1,e12}-8255S_{1,e13}+15541S_{1,e14}-45286=0$ |
| | $\psi_{83}^{upper}$ | $10228S_{1,e2}+5215S_{1,e3}+17530S_{1,e4}-22251S_{1,e5}-45130S_{1,e6}+12553S_{1,e9}+30581S_{1,e10}+14523S_{1,e11}-12544S_{1,e12}-65328S_{1,e13}+1750S_{1,e14}-50487=0$ |
| Lower boundary | $\psi_1^{lower}$ | $12521S_{1,e2}+1170S_{1,e3}-5510S_{1,e4}-15781S_{1,e5}+7185S_{1,e6}+14511S_{1,e9}+20521S_{1,e10}-33860S_{1,e11}+2021S_{1,e12}-11496S_{1,e13}+44543S_{1,e14}-210237=0$ |
| | $\psi_2^{lower}$ | $25518S_{1,e2}+8957S_{1,e3}-12002S_{1,e4}-10553S_{1,e5}+6525S_{1,e6}+34101S_{1,e9}-9512S_{1,e10}-15135S_{1,e11}+10225S_{1,e12}-9055S_{1,e13}+1144S_{1,e14}+191109=0$ |
| | $\psi_3^{lower}$ | $19380S_{1,e2}+18512S_{1,e3}+15514S_{1,e4}-35224S_{1,e5}-31221S_{1,e6}+5285S_{1,e9}+64103S_{1,e10}+51125S_{1,e11}-8116S_{1,e12}-8824S_{1,e13}-21360S_{1,e14}+332801=0$ |
| | … | … |
| | $\psi_{45}^{lower}$ | $22510S_{1,e2}-12150S_{1,e3}+14251S_{1,e4}-51223S_{1,e5}+22315S_{1,e6}+34121S_{1,e9}+11305S_{1,e10}-33453S_{1,e11}-8512S_{1,e12}-13524S_{1,e13}-9853S_{1,e14}-273518=0$ |
| | $\psi_{46}^{lower}$ | $30102S_{1,e2}+31225S_{1,e3}+9213S_{1,e4}-42531S_{1,e5}+15138S_{1,e6}+32115S_{1,e9}-54111S_{1,e10}-2053S_{1,e11}+7712S_{1,e12}-25158S_{1,e13}-13523S_{1,e14}-312011=0$ |

### 2) Observation of EPS-ECSR

Fig. 3 exemplarily illustrates the observation results of EPS-ECSR. Fig. 3(a) selects $S_{1,e12}$ and $S_{1,e14}$ as observation variables, visualizing the 2D view of EPS-ECSR under fixed parameters: $S_{1,e2}$=20MVA, $S_{1,e3}$=90MVA, $S_{1,e4}$=40MVA, $S_{1,e5}$=5MVA, $S_{1,e6}$=10MVA, $S_{1,e9}$=20MVA, $S_{1,e10}$=10MVA, $S_{1,e11}$=5MVA and $S_{1,e13}$=5MVA. Fig. 3(b) selects $S_{1,e3}$, $S_{1,e4}$ and $S_{1,e10}$ as observation variables, visualizing the 3D view of EPS-ECSR under fixed parameters: $S_{1,e2}$=20MVA, $S_{1,e5}$=5MVA, $S_{1,e6}$=10MVA, $S_{1,e9}$=25MVA, $S_{1,e10}$=10MVA, $S_{1,e11}$=5MVA, $S_{1,e13}$=5MVA and $S_{1,e13}$=13MVA. Fig 3(c) shows the full-dimensional observation view of EPS-ECSR: the red line represents the upper boundary of the full-dimensional view, and the blue line represents the lower boundary.
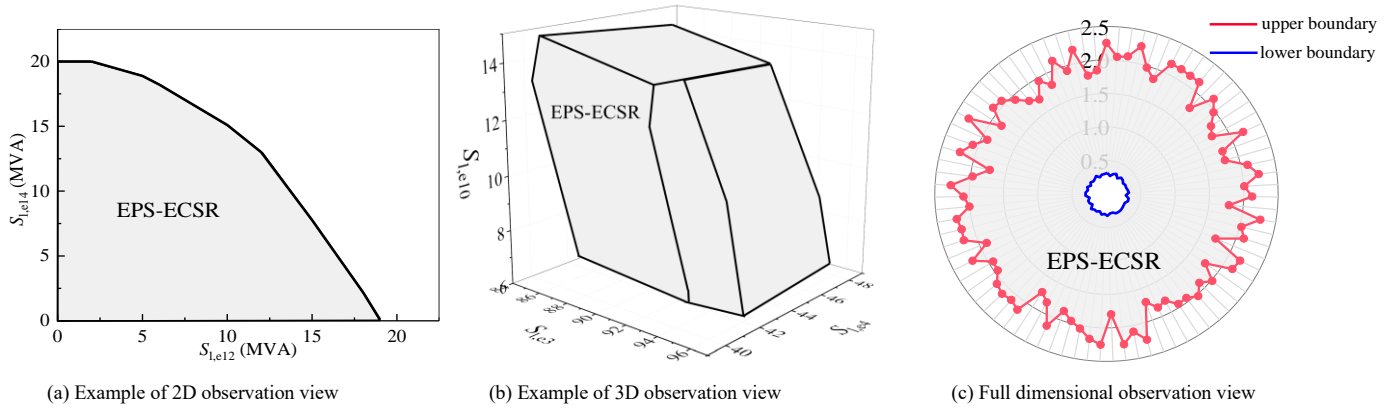


(a) Example of 2D observation view     (b) Example of 3D observation view     (c) Full dimensional observation view

Fig. 3. observation results of EPS-ECSR of IEEE 14-bus system

### B. Solution and observation of NGS-ECSR

### 1) Solution of NGS -ECSR

The parameter settings for boundary point calculation are as follows: in the state space, loads of nodes $N_{g3}$, $N_{g5}$, and $N_{g8}$ are sampled at equal intervals with a sampling step size of 5m$^3$/s; the load of $N_{g9}$, i.e. $G_{1,g9}$ is modified, the convergence accuracy of modify step size is 0.01m$^3$/s.

The NGS-ECSR modeling results are detailed in Sections 5.2.2 and 5.3.2 of Ref. [28] or Appendix B of this paper. The specific solution procedure is described below.

First, perform security verification on the operating point as follows. The operating point to be validated is substituted into equation (22) of Ref. [28] along with given state variables, all state variables of the operating point are obtained: If they satisfy the security constraints specified in equation (22), the operating point is considered secure; otherwise, it is insecure.

Second, according to the method in Section 3.2.2 to solve the security boundary points, the process is similar to that of EPS-ECSR, which will not be repeated here.

Finally, 338 upper boundary points are obtained, as shown in Table VI. There is only one point on the lower boundary, that is (69, 126, 0, 0), which is the intersection point of the lower limit of the state space boundary.
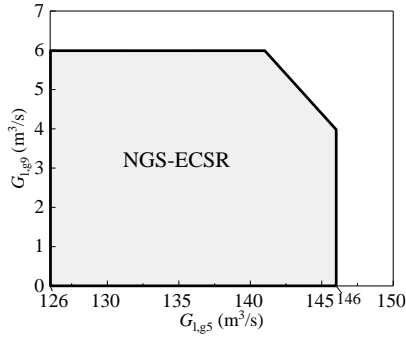
TABLE VI
UPPER BOUNDARY POINTS OF THE SOUTHEASTERN BELGIUM NATURAL GAS SYSTEM

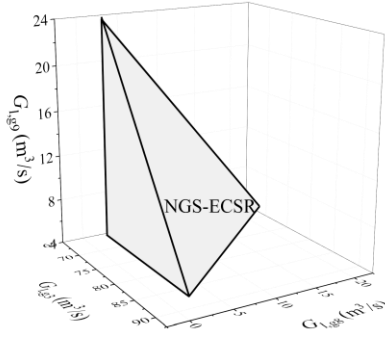| Upper boundary point | $(G_{l,g3}, G_{l,g5}, G_{l,g8}, G_{l,g9})$ |
|---|---|
| $W_{b,1}$ | (129, 126, 0, 4.87) |
| $W_{b,2}$ | (124, 131, 0, 5.21) |
| $W_{b,3}$ | (124, 126, 5, 5.33) |
| $W_{b,4}$ | (119, 136, 0, 5.45) |
| $W_{b,5}$ | (119, 131, 5, 5.61) |
| … | … |
| $W_{b,338}$ | (104, 126, 20, 6.77) |

Fit the security boundary using boundary points and set the distance error threshold to 0.1, 12 upper boundary hyperplanes are obtained, as shown in Table VII.

TABLE VII
EXPRESSION OF SECURITY BOUNDARY OF NGS-ECSR OF THE SOUTHEASTERN BELGIUM NATURAL GAS SYSTEM
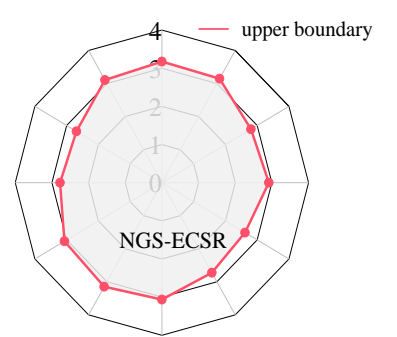
| | Hyperplane | Expression |
|---|---|---|
| Upper | $\psi_1^{upper}$ | $3142G_{l,g3}+734G_{l,g5}-5288G_{l,g8}+47G_{l,g9}-1951=0$ |
| boundary | $\psi_2^{upper}$ | $205G_{l,g3}-1154G_{l,g5}-1541G_{l,g8}+728G_{l,g9}-657=0$ |
| | $\psi_3^{upper}$ | $175G_{l,g3}+2281G_{l,g5}+674G_{l,g9}-850=0$ |
| | … | … |
| | $\psi_{11}^{upper}$ | $585G_{l,g3}+1125G_{l,g5}-598G_{l,g8}+1147G_{l,g9}-621=0$ |
| | $\psi_{12}^{upper}$ | $1087G_{l,g3}+1121G_{l,g5}-696G_{l,g8}-27G_{l,g9}-653=0$ |

*2) Observation of NGS-ECSR*

Fig. 4 exemplarily illustrates the observation results of NGS-ECSR. Fig. 4(a) selects $G_{l,g5}$, and $G_{l,g9}$ as observation variables, visualizing the 2D view of NGS-ECSR under fixed parameters: $G_{l,g3}=89m^3/s$, $G_{l,g8}=20m^3/s$. Fig. 4(b) selects $G_{l,g3}$, $G_{l,g8}$, and $G_{l,g9}$ as observation variables, visualizing the 3D view of NGS-ECSR under fixed parameters: $G_{l,g5}=166m^3/s$. Fig 4(c) shows the full-dimensional view of NGS-ECSR: the red line represents the upper boundary.



(a) Example of 2D observation view  (b) Example of 3D observation view  (c) Full dimensional observation view
Fig. 4. Observation results of NGS-ECSR of the southeastern Belgium natural gas system

*C.  Solution and observation of IES-ECSR*

*1)  Solution of IES-ECSR*

The parameter settings for boundary point calculation are as follows: the load of $N_{g9}$, i.e. $G_{l,g9}$ is modified, the convergence accuracy of modified step size is $0.01m^3/s$; and the remaining loads are sampled at equal intervals.

The IES-ECSR modeling results are detailed in Sections 5.2.3 and 5.3.3 of Ref. [28] or Appendix B of this paper. The specific solution procedure is described below.

First, the operating point to be validated is substituted into equation (23) of Ref. [28] along with given state variables, all state variables of the operating point are obtained: If they satisfy the security constraints specified in equation (23), the point is secure; otherwise, it is insecure.

Second, according to the method in Section 3.2.2 to solve the security boundary points, the process is similar to that of EPS-ECSR, which will not be repeated here.

Finally, 10513152 upper boundary points and 4725166 lower boundary points are obtained, as shown in Table VIII.

TABLE VIII
UPPER AND LOWER BOUNDARY POINTS IN IES-ECSR OF 23-NODE IES

| | | $(S_{l,e2},S_{l,e3},S_{l,e4},S_{l,e5},S_{l,e6},S_{l,e9},S_{l,e10},S_{l,e11},S_{l,e12},S_{l,e13},S_{l,e14},S_{l,c1},S_{l,c2},S_{l,c3},G_{l,g3},G_{l,g5},G_{l,GT1},G_{l,g8},G_{l,GT2},G_{l,g9})$ |
|---|---|---|
| Upper boundary point | $W_{b,1}$ | (20, 85, 40, 0, 0, 25, 0, 0, 0, 0, 10, 2, 2, 5, 69, 126, 10, 0, 5, 15.7422) |
| | $W_{b,2}$ | (20, 85, 40, 0, 0, 25, 0, 0, 0, 0, 10, 2, 2, 5, 69, 126, 10, 0, 10, 10.7419) |
| | $W_{b,3}$ | (20, 85, 40, 0, 0, 25, 0, 0, 0, 0, 10, 2, 2, 5, 69, 126, 10, 0, 15, 5.7408) |
| | $W_{b,4}$ | (20, 85, 40, 0, 0, 25, 0, 0, 0, 0, 10, 2, 2, 5, 69, 126, 10, 0, 20, 0.7382) |
| | $W_{b,5}$ | (20, 85, 40, 0, 0, 25, 0, 0, 0, 0, 10, 2, 2, 5, 69, 126, 10, 5, 5, 10.7419) |
| | … | … |
| | $W_{b,10513152}$ | (30, 100, 55, 10, 15, 40, 10, 5, 10, 5, 10, 4, 4, 3, 129, 126, 40, 0, 10, 4.4512) |
| Lower boundary point | $W_{b,1}$ | (20, 85, 40, 0, 0, 25, 0, 0, 0, 0, 10, 3, 3, 1, 69, 126, 10, 0, 5, 1.1266) |
| | $W_{b,2}$ | (20, 85, 40, 0, 0, 25, 0, 0, 0, 0, 10, 3, 3, 1, 69, 126, 10, 0, 10, 1.1269) |
| | $W_{b,3}$ | (20, 85, 40, 0, 0, 25, 0, 0, 0, 0, 10, 3, 3, 1, 69, 126, 10, 0, 15, 1.1281) |
| | $W_{b,4}$ | (20, 85, 40, 0, 0, 25, 0, 0, 0, 0, 10, 3, 3, 1, 69, 126, 10, 0, 20, 1.1304) |
| | $W_{b,5}$ | (20, 85, 40, 0, 0, 25, 0, 0, 0, 0, 10, 3, 3, 1, 69, 126, 10, 5, 5, 1.1269) |
| | … | … |
| | $W_{b,4725166}$ | (30, 85, 50, 10, 15, 20, 10, 0, 10, 0, 10, 2, 2, 3, 94, 126, 15, 10, 10, 2.0852) |

Fit the security boundary using boundary points and set the distance error threshold to 0.5, 1183 upper boundary hyperplanes and 485 lower boundary hyperplanes are obtained, as shown in Table IX.

TABLE IX
EXPRESSION OF SECURITY BOUNDARY OF IES-ECSR OF 23-NODE IES

| Hyperplane | | Expression |
|---|---|---|
| Upper boundary | $\psi_1^{upper}$ | $1684S_{1,e2}+4580S_{1,e3}-48048S_{1,e4}-60269S_{1,e5}-60269S_{1,e6}-76290S_{1,e9}+974575S_{1,e10}-9909S_{1,e11}+49543S_{1,c2}-196S_{1,c3}-150G_{1,g3}+8444G_{1,g5}-28906G_{1,GT1}-24462G_{1,g8}-24025G_{1,GT2}+3648G_{1,g9}+82505=0$ |
| | $\psi_2^{upper}$ | $1744S_{1,e2}+2423S_{1,e3}-49764S_{1,e4}-45127S_{1,e5}-45127S_{1,e6}-57122S_{1,e9}+739886S_{1,e10}+32760S_{1,e12}+280730S_{1,e13}+280730S_{1,e14}+355354S_{1,c1}-4574960S_{1,c2}+145S_{1,c3}+96G_{1,g3}-4134G_{1,g5}+7158G_{1,GT1}+4027G_{1,g8}+1954G_{1,GT2}-994G_{1,g9}+461611=0$ |
| | $\psi_3^{upper}$ | $1649S_{1,e2}-7369S_{1,e3}-47060S_{1,e4}-160236S_{1,e5}-160236S_{1,e6}-125098S_{1,e9}+2274731S_{1,e10}-61928S_{1,e13}+61928S_{1,c2}+183S_{1,c3}+156G_{1,g3}-5233G_{1,g5}+22864G_{1,GT1}+18556G_{1,g8}+17225G_{1,GT2}-2736G_{1,g9}-211851=0$ |
| | $\psi_4^{upper}$ | $4089S_{1,e3}+275237S_{1,e5}-275237S_{1,e6}+275237S_{1,e9}-4132483S_{1,e10}-32760S_{1,e12}+50537S_{1,e13}+112466S_{1,e14}+37841S_{1,c1}-703914S_{1,c2}+712S_{1,c3}+535G_{1,g3}-20306G_{1,g5}+69136G_{1,GT1}+59577G_{1,g8}+56396G_{1,GT2}-7935G_{1,g9}+396154=0$ |
| | $\psi_5^{upper}$ | $-330S_{1,e2}-3528S_{1,e3}+9412S_{1,e4}-59331S_{1,e5}-59331S_{1,e6}-37892S_{1,e9}+794629S_{1,e10}-9800S_{1,e11}-131040S_{1,e12}-20793S_{1,e13}-20793S_{1,e14}+77050S_{1,c1}-74853S_{1,c2}+906S_{1,c3}+548 G_{1,g3}-25864G_{1,g5}+69721G_{1,g8}+66653G_{1,GT2}-1188G_{1,g9}-83923=0$ |
| | … | |
| | $\psi_{1183}^{upper}$ | $3716S_{1,e3}+129656S_{1,e5}+147448S_{1,e6}+147448S_{1,e9}-2203664S_{1,e10}+282160S_{1,e11}+282160S_{1,e12}-91448S_{1,e13}-91448S_{1,e14}-115757S_{1,c1}+1425254S_{1,c2}+198S_{1,c3}-11G_{1,g3}-5655G_{1,g5}+26511G_{1,g8}+27222G_{1,GT2}-4087G_{1,g9}+245228=0$ |
| Lower boundary | $\psi_1^{lower}$ | $-2889S_{1,e2}+722S_{1,e3}+536768S_{1,e4}+190562S_{1,e5}-234487S_{1,e6}-355404S_{1,e9}+2406165S_{1,e10}+1630S_{1,e11}-4324S_{1,e12}+231522S_{1,e13}-66871S_{1,e14}-79826S_{1,c2}-77080S_{1,c3}+30G_{1,g5}+824G_{1,GT1}+3818G_{1,g8}-3666G_{1,GT2}+3214G_{1,g9}+1502312=0$ |
| | $\psi_2^{lower}$ | $1894S_{1,e2}-473S_{1,e3}-46744S_{1,e5}-49955S_{1,e6}-71262S_{1,e9}+507846S_{1,e10}+509S_{1,e12}-269082S_{1,e13}+93700S_{1,e14}+89584S_{1,c1}+109278S_{1,c2}-823141S_{1,c3}+84G_{1,g3}-2718G_{1,g5}+21749G_{1,GT1}-9710G_{1,g8}-8803G_{1,GT2}+11780G_{1,g9}+608589=0$ |
| | $\psi_3^{lower}$ | $3536S_{1,e2}-884S_{1,e3}-552258S_{1,e4}+220078S_{1,e5}+266427S_{1,e6}+380065S_{1,e9}-2756002S_{1,e10}+194S_{1,e11}+370S_{1,e12}+10930S_{1,e13}-20754S_{1,e14}-23330S_{1,c1}-14972S_{1,c2}+204236S_{1,c3}-18G_{1,g3}-911G_{1,g5}+16818G_{1,GT1}-7080G_{1,g8}-5599G_{1,GT2}-6830G_{1,g9}+1547384=0$ |
| | $\psi_4^{lower}$ | $-5206S_{1,e2}-3812S_{1,e3}+905712S_{1,e4}-334435S_{1,e5}-420248S_{1,e6}+4319855S_{1,e10}-1338S_{1,e11}-2812S_{1,e12}-27277S_{1,e13}+29584S_{1,c1}+42837S_{1,c2}-284519S_{1,c3}-184G_{1,g3}-1250G_{1,g5}+8983G_{1,GT1}-4404G_{1,g8}-2736G_{1,GT2}+5220G_{1,g9}+2250848=0$ |
| | $\psi_5^{lower}$ | $1345S_{1,e2}-336S_{1,e3}+196363S_{1,e4}-80578S_{1,e5}-102503S_{1,e6}-117636S_{1,e9}+851761S_{1,e10}-1775S_{1,e11}-3843S_{1,e12}+32497S_{1,e14}+35409S_{1,c1}+31295S_{1,c2}-197537S_{1,c3}-1306G_{1,g5}+101664G_{1,GT2}+13195G_{1,g9}-611994=0$ |
| | … | … |
| | $\psi_{485}^{lower}$ | $119357S_{1,e2}+127277S_{1,e3}+21917S_{1,e4}-21917S_{1,e9}-2029S_{1,e10}-4392S_{1,e11}-18122S_{1,e12}+24483S_{1,e13}+40467S_{1,e14}+35766S_{1,c1}-213100S_{1,c2}+185S_{1,c3}+6220G_{1,g3}-88614G_{1,g5}+34277G_{1,GT1}+32002G_{1,GT2}+4074G_{1,g9}-193786=0$ |

## 2) Observation of IES-ECSR

Fig. 5 exemplarily illustrates the observation results of IES-ECSR. Fig. 5(a) selects $G_{1,g3}$ and $G_{1,g5}$ as observation variables, visualizing the 2D view of IES-ECSR with other loads at (20, 85, 45, 0, 5, 25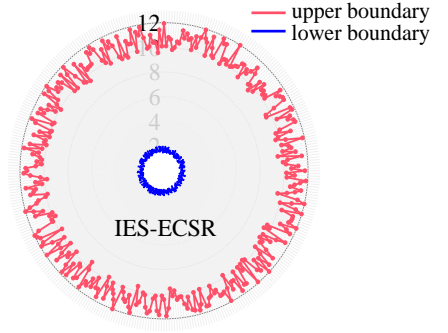, 0, 0, 0, 0, 10, 2, 2, 3, 10, 0, 5, 5); Fig. 5(b) selects $S_{1,e12}$, $S_{1,e13}$ and $S_{1,e14}$ as observation variables, visualizing the 3D view of IES-ECSR with other loads at (25, 85, 50, 0, 5, 25, 10, 0, 10, 2, 2, 5, 69, 126, 10, 0, 5, 5); Fig 5(c) shows the full dimensional view of IES-ECSR: the red line represents the upper boundary, the blue line represents the lower boundary.
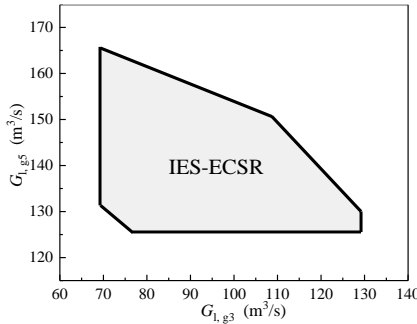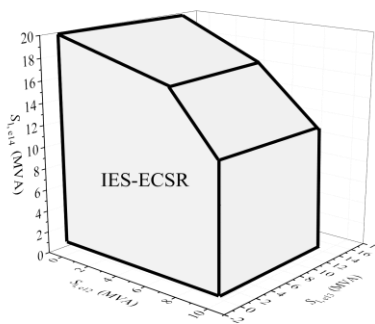


(a) Example of 2D observation view     (b) Example of 3D observation view     (c) Full dimensional observation view
Fig. 5.    observation results of IES-ECSR of the 23-node IES

## D. Comparison with existing methods

Ref. [11] first proposed the concept and model of security region for IES. The subsequent related research [12-15] extended the IES-SR based on [11], while the basic models are not fundamentally different from [11]: all are based on the inherent energy flow equation of heterogeneous energy. Therefore, this section takes the IES case as an example and selects the method of [11] as the traditional method for comparative verification.

First, Table X compares the calculation results of security boundary points of the proposed method and traditional methods. It can be seen that the error of the proposed method is very small: the number of boundary points obtained is the same as that of the traditional method and corresponds to each other; the deviation of boundary points is very small, with the maximum relative deviation being only 0.026%.

The reason for the error is small is that the base value of pipeline flow is introduced in the ECSR modeling: if the base value is equal to the actual flow rate, the network equation in this paper is equivalent to the pipeline pressure drop equation, there is no error in theory. In this paper, the base value determination methods of papers [21-22] are adopted, which can effectively control the error.

TABLE X

COMPARISON OF THE SOLUTION RESULTS OF BOUNDARY POINTS OF THE IES SECURITY REGION

| | | Operating points $(S_{1,e2},S_{1,e3},S_{1,e4},S_{1,e5},S_{1,e6},S_{1,e9},S_{1,e10},S_{1,e11},S_{1,e12},S_{1,e13},S_{1,e14},S_{1,c1},S_{1,c2},S_{1,c3},$ $G_{1,g3},G_{1,g5},G_{1,GT1},G_{1,g8},G_{1,GT2},G_{1,g9})$ | | |
|---|---|---|---|---|
| | | Traditional method [R2] | Proposed method | Relative deviation |
| Upper boundary point | $W_{b,1}$ | (20, 85, 40, 0, 0, 25, 0, 0, 0, 0, 10, 2, 2, 5, 69, 126, 10, 0, 5, 15.7422) | (20, 85, 40, 0, 0, 25, 0, 0, 0, 0, 10, 2, 2, 5, 69, 126, 10, 0, 5, 15.7421) | 0.001% |
| | $W_{b,2}$ | (20, 85, 40, 0, 0, 25, 0, 0, 0, 0, 10, 2, 2, 5, 69, 126, 10, 0, 10, 10.7419) | (20, 85, 40, 0, 0, 25, 0, 0, 0, 0, 10, 2, 2, 5, 69, 126, 10, 0, 10, 10.7418) | 0.001% |
| | $W_{b,3}$ | (20, 85, 40, 0, 0, 25, 0, 0, 0, 0, 10, 2, 2, 5, 69, 126, 10, 0, 15, 5.7408) | (20, 85, 40, 0, 0, 25, 0, 0, 0, 0, 10, 2, 2, 5, 69, 126, 10, 0, 15, 5.7408) | - |
| | $W_{b,4}$ | (20, 85, 40, 0, 0, 25, 0, 0, 0, 0, 10, 2, 2, 5, 69, 126, 10, 0, 20, 0.7382) | (20, 85, 40, 0, 0, 25, 0, 0, 0, 0, 10, 2, 2, 5, 69, 126, 10, 0, 20, 0.7381) | 0.014% |
| | $W_{b,5}$ | (20, 85, 40, 0, 0, 25, 0, 0, 0, 0, 10, 2, 2, 5, 69, 126, 10, 5, 5, 10.7419) | (20, 85, 40, 0, 0, 25, 0, 0, 0, 0, 10, 2, 2, 5, 69, 126, 10, 5, 5, 10.7418) | 0.001% |
| | … | … | … | |
| | $W_{b,10513152}$ | (30, 100, 55, 10, 15, 40, 10, 5, 10, 5, 10, 4, 4, 3, 129, 126, 40, 0, 10, 4.4512) | (30, 100, 55, 10, 15, 40, 10, 5, 10, 5, 10, 4, 4, 3, 129, 126, 40, 0, 10, 4.4511) | 0.022% |
| Lower boundary point | $W_{b,1}$ | (20, 85, 40, 0, 0, 25, 0, 0, 0, 0, 10, 3, 3, 1, 69, 126, 10, 0, 5, 1.1266) | (20, 85, 40, 0, 0, 25, 0, 0, 0, 0, 10, 3, 3, 1, 69, 126, 10, 0, 5, 1.1265) | 0.009% |
| | $W_{b,2}$ | (20, 85, 40, 0, 0, 25, 0, 0, 0, 0, 10, 3, 3, 1, 69, 126, 10, 0, 10, 1.1269) | (20, 85, 40, 0, 0, 25, 0, 0, 0, 0, 10, 3, 3, 1, 69, 126, 10, 0, 10, 1.1268) | 0.009% |
| | $W_{b,3}$ | (20, 85, 40, 0, 0, 25, 0, 0, 0, 0, 10, 3, 3, 1, 69, 126, 10, 0, 15, 1.1281) | (20, 85, 40, 0, 0, 25, 0, 0, 0, 0, 10, 3, 3, 1, 69, 126, 10, 0, 15, 1.1280) | 0.009% |
| | $W_{b,4}$ | (20, 85, 40, 0, 0, 25, 0, 0, 0, 0, 10, 3, 3, 1, 69, 126, 10, 0, 20, 1.1304) | (20, 85, 40, 0, 0, 25, 0, 0, 0, 0, 10, 3, 3, 1, 69, 126, 10, 0, 20, 1.1303) | 0.009% |
| | $W_{b,5}$ | (20, 85, 40, 0, 0, 25, 0, 0, 0, 0, 10, 3, 3, 1, 69, 126, 10, 5, 5, 1.1269) | (20, 85, 40, 0, 0, 25, 0, 0, 0, 0, 10, 3, 3, 1, 69, 126, 10, 5, 5, 1.1268) | 0.008% |
| | … | … | … | … |
| | $W_{b,2951428}$ | (25, 85, 40, 0, 0, 25, 0, 0, 0, 0, 10, 2, 2, 1, 94, 131, 15, 0, 5, 0.3825) | (25, 85, 40, 0, 0, 25, 0, 0, 0, 0, 10, 2, 2, 1, 94, 131, 15, 0, 5, 0.3824) | 0.026% |
| | … | … | … | |
| | $W_{b,4725166}$ | (30, 85, 50, 10, 15, 20, 10, 0, 10, 0, 10, 2, 2, 3, 94, 126, 15, 10, 10, 2.0852) | (30, 85, 50, 10, 15, 20, 10, 0, 10, 0, 10, 2, 2, 3, 94, 126, 15, 10, 10, 2.0851) | 0.005% |

Note: (1) Blue marks the deviation and maximum deviation generated when solving boundary points.

(2) To observe the relative deviation between the results of this paper and those of the traditional method, the accuracy of boundary points is improved to $10^{-4}$ in the table

Second, compared with the existing method, this method has two advantages as follows.

**Advantage 1**: High solution efficiency at security boundary points.

In solving boundary points, existing methods take 136.58 hours, while the proposed method takes 2.92 hours, resulting in a 46.77-fold increase in efficiency. The reason is that when using energy circuit modeling for the security region, the momentum conservation equation of the natural gas flow process is linearized, avoiding the iterative process of solving the pipeline pressure drop equation.

**Advantage 2:** In terms of the security boundary analytical formula, complete full-dimensional boundary expressions can be obtained.

This paper depicts the complete security boundary of high-dimensional IES through full-dimensional security boundary expressions and full-dimensional security region views; while the existing method only obtains dimensionality reduction results, they are two-dimensional/three-dimensional cross-sectional views and the corresponding boundary expressions, these results only depict a small number of local security boundaries.

In security analysis, Advantage 2 means the ability to directly analyze the security of any operating point in a high-dimensional state space, obtaining the security margin of the operating point in all directions of the state space. The existing method can only perform security analysis on operating points located on the reduced dimensional sections, it can only obtain security margins in the dimension direction of the section. Existing methods cannot securely analyze operating points that are not located on the reduced dimensional section. If security analysis is required, additional calculations are needed as follows: first, fix some variables in the state space where the operating point is located; second, fit the corresponding security boundary section. These operations essentially involve recalculating the security boundary, which will lose the advantage of the online security analysis speed of the region.

Taking the 23-node IES as an example to further explain. First, randomly generate operating points $W_1 \sim W_{10}$. Second, the full dimensional security boundary is calculated and the reduced dimensional sections of the existing method are taken respectively to analyze the security of $W_1 \sim W_{10}$. Due to these points not being on the reduced dimensional section, the traditional method cannot analyze them, which means additional calculations are required. The Comparison results are shown in Table XI. It can be seen although the same analysis results are obtained based on two methods, the calculation time of the proposed method is reduced by $10^6$ times.

TABLE XI
COMPARISON OF ONLINE SECURITY ANALYSIS FOR RANDOM OPERATING POINTS OF 23-NODE IES

| Operating point | $(S_{1,e2},S_{1,e3},S_{1,e4},S_{1,e5},S_{1,e6},S_{1,e9},S_{1,e10},S_{1,e11},S_{1,e12},S_{1,e13},S_{1,e14},S_{1,c1},S_{1,c2},S_{1,c3},$ $G_{1,g3},G_{1,g5},G_{1,GT1},G_{1,g8},G_{1,GT2},G_{1,g9})$ | Proposed method | | Traditional method | |
|---|---|---|---|---|---|
| | | analysis result | time/s | analysis result | time/s |
| $W_1$ | (29.45, 96.58, 54.64, 5.67, 7.07, 28.81, 12.85, 0.66, 5.27, 7.19, 18.28, 134.0, 2.3, 28.05) | secure | $8.54\times10^{-3}$ | secure | $1.87\times10^3$ |
| $W_2$ | (27.14, 92.13, 48.33, 9.69, 8.14, 26.99, 13.5, 4.35, 8.94, 13.48, 15.07, 154.8, 22.22, 8.48) | insecure | $8.11\times10^{-3}$ | insecure | $1.68\times10^3$ |
| $W_3$ | (26.79, 95.21, 52.69, 8.25, 0.9, 33.18, 3.27, 3.01, 7.78, 14.02, 13.66, 184.4, 13.7, 4.09) | insecure | $7.62\times10^{-3}$ | insecure | $1.79\times10^3$ |
| $W_4$ | (29.59, 91.25, 46.12, 9.6, 9.87, 37.42, 1.15, 1.33, 0.69, 12.27, 12.27, 149.0, 20.05, 42.85) | insecure | $7.98\times10^{-3}$ | insecure | $1.64\times10^3$ |
| $W_5$ | (27.75, 90.7, 46.93, 6.46, 13.34, 37.56, 7.11, 4.32, 2.79, 10.63, 15.35, 133.8, 20.98, 18.48) | secure | $8.36\times10^{-3}$ | secure | $1.69\times10^3$ |
| $W_6$ | (26.08, 88.2, 52.39, 3.8, 1.64, 37.5, 12.53, 0.29, 3.79, 11.15, 12.89, 163.0, 17.14, 40.27) | insecure | $7.47\times10^{-3}$ | insecure | $1.99\times10^3$ |
| $W_7$ | (29.48, 90.74, 54.87, 4.77, 6.57, 28.06, 7.04, 2.29, 8.65, 13.5, 10.68, 182.9, 18.86, 39.15) | secure | $7.55\times10^{-3}$ | secure | $1.81\times10^3$ |
| $W_8$ | (20.6, 85.45, 47.86, 9.12, 4.2, 33.17, 6.21, 3.61, 4.2, 0.98, 10.85, 148.7, 26.33, 31.86) | insecure | $8.02\times10^{-3}$ | insecure | $1.82\times10^3$ |
| $W_9$ | (22.69, 92.08, 53.88, 0.15, 14.78, 38.12, 7.54, 1.7, 2.4, 5.04, 10.68, 128.7, 19.87, 42.91) | insecure | $7.96\times10^{-3}$ | insecure | $1.78\times10^3$ |
| $W_{10}$ | (29.87, 90.0, 51.09, 1.57, 9.13, 26.82, 1.88, 2.01, 5.98, 0.07, 14.1, 135.2, 26.26, 30.29) | insecure | $8.17\times10^{-3}$ | insecure | $1.80\times10^3$ |

## VI. Conclusion

To address the inconsistency in region modeling caused by diverse physical transmission processes and mathematical representations of heterogeneous energy systems, this paper series proposes the EPSR. As Part II of the series, this paper focuses on the calculation and observation of ECSR.

(1) A universal solution method is proposed, enabling full-dimensional security region determination for both single-energy systems and IES.

(2) A generalized visualization approach is developed, achieving dimensionality reduction and full-dimensional observation of high-dimensional ECSRs.

(3) The complete closed-form expression of full-dimensional security boundaries is derived for large-scale IES for the first time. Compared with existing methods, the proposed approach demonstrates two orders of magnitude improvement in boundary calculation efficiency within acceptable accuracy thresholds, as well as six orders of magnitude acceleration in security analysis, which truly enables online security analysis of region method.

The proposed ECSR has been validated through large-scale IES cases, EPS cases, and NGS cases, which can be further extended to other forms of energy systems or IES. The next work will focus on the dynamic processes of IES, as well as the ECSR considering multiple time scales.

## Acknowledgment

## References

[1] E. Hnyilicza, S. T. Y. Lee, and F. C. Schweppe, "Steady-state security regions: Set-theoretic approach," in *Proc. PICA Conf.*, New Orleans, LA, USA, 1975, pp. 347-355.

[2] F. Wu and S. Kumagai, "Steady-state security regions of power systems," *IEEE Trans. Circuits Syst.*, vol. 29, no. 11, pp. 703-711, Nov. 1982. DOI: 10.1109/TCS.1982.1085091.

[3] J. Xiao, W. Gu, C. Wang, and F. Li, "Distribution system security region: Definition, model and security assessment," *IET Gener. Transm. Distrib.*, vol. 6, no. 10, pp. 1029–1035, Oct. 2012. DOI: 10.1049/iet-gtd.2011.0767.

[4] Y. Yu, Y. Liu, C. Qin, and T. Yang, "Theory and method of power system integrated security region irrelevant to operation states: An introduction," *Engineering*, vol. 6, no. 7, pp. 754-777, Jul. 2020. DOI: 10.1016/j.eng.2019.11.016.

[5] J. Xiao, G. Zu, X. Gong, and C. Wang, "Model and topological characteristics of power distribution system security region," *J. Appl. Math.*, vol. 2014, no. 6, pp. 1-13, 2014. DOI: 10.1155/2014/327078.

[6] J. Xiao, G. Zu, Y. Wang, X. Zhang, and X. Jiang, "Model and observation of dispatchable region for flexible distribution network," *Appl. Energy*, vol. 261, 114425, pp. 1-9, Mar. 2020. DOI: 10.1016/j.apenergy.2019.114425.

[7] J. Xiao, Z. Qiu, G. Zu, C. Song, and X. Zhang, "Application of geometrical observation of security region in distribution network enhancement," *Int. Trans. Electr. Energy Syst.*, vol. 31, no. 11, e13030, Aug. 2021. DOI:10.1002/2050-7038.13030.

[8] C. Song, J. Xiao, G. Zu, Z. Hao, and X. Zhang, "Security region of natural gas pipeline network system: Concept, method and application," *Energy*, vol. 217, Feb. 2021, Art. no. 119283. DOI: 10.1016/j.energy.2020.119283.

[9] X. Li, G. Tian, Q. Shi, T. Jiang, F. Li, and H. Jia, "Security region of natural gas network in electricity-gas integrated energy system," *Int. J. Electr. Power Energy Syst.*, vol. 117, May 2020, Art. no. 105601. DOI: 10.1016/j.ijepes.2019.105601.

[10] H. Dong, Z. Han, J. Zhao, and W. Wang, "A dynamic security region construction method and its existence proof for gaseous system," *Appl. Energy*, vol. 367, Aug. 2024, Art. no. 123213. DOI: 10.1016/j.apenergy.2024.123213.

[11] S. Chen, Z. Wei, G. Sun, Y. Sun, and N. Lu, "Steady-state security regions of electricity-gas integrated energy systems," in *Proc. IEEE Power and Energy Society General Meeting*, Boston, MA, USA, 2016, pp. 1-5. DOI: 10.1109/PESGM.2016.7741474.

[12] S. Chen, Z. Wei, G. Sun, W. Wei, and D. Wang, "Convex hull based robust security region for electricity-gas integrated energy systems," *IEEE Trans. Power Syst.*, vol. 34, no. 3, pp. 1740-1748, May 2019. DOI:10.1109/TPWRS.2018.2888605.

[13] T. Jiang, R. Zhang, X. Li, H. Chen, and G. Li, "Integrated energy system security region: concepts, methods, and implementations," *Appl. Energy*, vol. 283, Feb. 2021, Art. no. 116124. DOI: 10.1016/j.apenergy.2020.116124.

[14] L. Liu, D. Wang, K. Hou, H. Jia, and S. Li, "Region model and application of regional integrated energy system security analysis," *Appl. Energy*, vol. 260, Feb. 2020, Art. no. 114268. DOI: 10.1016/j.apenergy.2019.114268.

[15] P. Yong, Y. Wang, T. Capuder, Z. Tan, N. Zhang, and C. Kang, "Steady-state security region of energy hub: Modeling, calculation, and applications," *Int. J. Electr. Power Energy Syst.*, vol. 125, Feb. 2021, Art. no. 106551. DOI: 10.1016/j.ijepes.2020.106551.

[16] J. Su, H. Chiang, and L. F. C. Alberto, "Two-time-scale approach to characterize the steady-state security region for the electricity-gas integrated energy system," *IEEE Trans. Power Syst.*, vol. 36, no. 6, pp. 5863-5873, Nov. 2021. DOI: 10.1109/TPWRS.2021.3081700.

[17] J. Su, H. Chiang, Y. Zeng, and N. Zhou, "Toward complete characterization of the steady-state security region for the electricity-gas integrated energy system," *IEEE Trans. Smart Grid*, vol. 12, no. 4, pp. 3004-3015, Mar. 2021. DOI: 10.1109/TSG.2021.3065501.

[18] Z. Xiong, C. Zhang, D. Qiu, L. Wang, C. Jiang, and S. Zhou, "Feasible region identification approach for the regional integrated energy system considering flexible ramping constraints based on polyhedral projection algorithm," *Int. J. Electr. Power Energy Syst.*, vol. 163, Dec. 2024, Art. no. 110347. DOI: 10.1016/j.ijepes.2024.110347.

[19] B. Chen, Q. Guo, G. Yin, B. Wang, Z. Pan, Y. Chen, et al., "Energy-circuit-based integrated energy management system: Theory, implementation, and application," *Proc. IEEE*, vol. 110, no. 12, pp. 1897–1926, Dec. 2022. DOI: 10.1109/JPROC.2022.3216567.

[20] B. Chen, W. Wu, Q. Guo, and H. Sun, "An efficient optimal energy flow model for integrated energy systems based on energy circuit modeling in the frequency domain," *Appl. Energy*, vol. 326, Nov. 2022, Art. no. 119923. DOI: 10.1016/j.apenergy.2022.119923.

[21] B. Chen, H. Sun, Y. Chen, W. Wu, and Z. Qiao, "Energy circuit theory of integrated energy system analysis (I): Gaseous circuit," *Proc. CSEE (in Chinese)*, vol. 40, no. 2, pp. 436-444, Jan. 2020. DOI: 10.13334/j.0258-8013.pcsee.200028.

[22] B. Chen, H. Sun, W. Wu, Q. Guo, and Z. Qiao, "Energy circuit theory of integrated energy system analysis (III): Steady and dynamic energy flow calculation," *Proc. CSEE (in Chinese)*, vol. 40, no. 15, pp. 4820-4831, Jul. 2020. DOI: 10.13334/j.0258-8013.pcsee.200647.

[23] J. Yang, N. Zhang, A. Botterud, and C. Kang, "Situation awareness of electricity-gas coupled systems with a multi-port equivalent gas network model," *Appl. Energy*, vol. 258, Jan. 2020, Art. no. 114029. DOI: 10.1016/j.apenergy.2019.114029.

[24] J. Yang, N. Zhang, and C. Kang, "Analysis theory of generalized electric circuit for multi-energy networks—Part one: Branch model," *Autom. Electr. Power Syst. (in Chinese)*, vol. 44, no. 9, pp. 21-32, May 2020. DOI: 10. 7500/AEPS20200209001.

[25] J. Yang, N. Zhang, and C. Kang, "Analysis theory of generalized electric circuit for multi-energy networks—Part two: Network model," *Autom. Electr. Power Syst. (in Chinese)*, vol. 44, no. 10, pp. 10-21, May 2020. DOI: 10. 7500/AEPS20200209002.

[26] L. Wang, J. Zheng, Z. Li, Z. Jing, and Q. Wu, "Order reduction method for high-order dynamic analysis of heterogeneous integrated energy systems," *Appl. Energy*, vol. 308, Feb. 2022, Art. no. 118265. DOI: 10.1016/j.apenergy.2021.118265.

[27] S. Zhang, W. Gu, S. Yao, S. Zhou, and Z. Wu, "Unified modeling of integrated energy networks in time domain and its applications (I): Two-part models in time domain," *Proc. CSEE (in Chinese)*, vol. 41, no. 19, pp. 6509-6521, Jul. 2021. DOI: 10.13334/j.0258-8013.pcsee.210486.

[28] J. Xiao, C. Wang, C. Song, X. Jiang, C. Li, and G. Sun, "Energy Circuit Security Region of Energy System (I): Concepts and Models," *IEEE Trans. Smart Grid*, 2025, under review.

[29] J. Deng, G. Wu, Y. Wang, Y. Su, and A. Liu, "Security-constrained hybrid optimal energy flow model of multi-energy system considering N-1 component failure," *J. Energy Storage*, vol. 64, Aug. 2023, Art. no. 107060. DOI: 10.1016/j.est.2023.107060.

[30] J. Xiao, Z. Qiu, C. Song, Z. Bao, H. Jiao, and Z. Lv, "Geometrical Observation Indices of Distribution System Security Region," in *Proc. IEEE I&CPS Asia*, 2021, pp. 1556-1561. DOI: 10.1109/ICPSAsia52756.2021.9621401.

[31] J. Xiao, Q. Lin, L. Bai, X. Zhang, L. Zuo, H. Zhou, et al., "Security distance for distribution system: Definition, calculation, and application," *Int. Trans. Electr. Energy Syst.*, vol. 29, no. 5, e2838, Feb 2019. DOI: 10.1002/2050-7038.2838

## APPENDIX

### A. Nomenclature

TABLE A2
DESCRIPTION OF THE MATHEMATICAL SYMBOLS IN THIS PAPER

| | Symbol | Meaning |
|---|---|---|
| | $W$ | Operating point |
| | $\Omega_{\text{EPS-ECSR}}$ | ECSR of EPS |
| | $S_{\text{l},ei}$ | power of power load node $i$ |
| | $S_{\text{l},cm}$ | power required to drive compressor $m$ |
| | $I_\text{n}$ | vector of node current |
| Symbols of EPS-ECSR | $I_\text{n}^{\max}$, $I_\text{n}^{\min}$ | vectors of the upper and lower limits of node current |
| | $I_\text{b}$ | vector of branch current |
| | $I_\text{b}^{\max}$ | vector of the current-carrying capacity |
| | $U_\text{n}$ | vector of node voltage |
| | $U_\text{n}^{\max}$, $U_\text{n}^{\min}$ | vectors of the upper and lower limits of node voltage |
| | $Y_\text{e}$ | node admittance matrix of EPS |
| | $K_\text{e}$ | transformer ratio matrix |
| | $\Omega_{\text{NGS-ECSR}}$ | ECSR of NGS |
| | $G_{\text{l},gj}$ | flow rate of natural gas load node $j$ |
| | $G_{\text{l,GT}n}$ | natural gas input by the gas generator $n$ |
| | $G_\text{n}$ | vectors of node flow of natural gas |
| | $G_\text{n}^{\max}$, $G_\text{n}^{\min}$ | vector of the upper and lower limits of the node gas flow |
| Symbols of NGS-ECSR | $p_\text{n}$ | vector of node pressure of natural gas |
| | $p_\text{n}^{\max}$, $p_\text{n}^{\min}$ | vector of the upper and lower limits of node pressure |
| | $G_\text{b}^{\max}$ | vector of pipe capacity |
| | $K_\text{g}$ | matrix of compressor pressure ratio |
| | $Y_\text{g}$ | generalized node admittance matrix of NGS |
| | $A_{\text{g, L}}^{-1}$ | Left inverse matrix of $A_\text{g}$ |
| | $\Omega_{\text{IES-ECSR}}$ | ECSR of IES |
| | $P_\text{n}$ | vector of node pressure of natural gas |
| | $P_\text{n}^{\max}$, $P_\text{n}^{\min}$ | vector of the upper and lower limits of node pressure |
| | $F_\text{n}$ | vector of energy flow |
| | $F_\text{b}^{\max}$ | vector of the upper limits of node flow |
| | $Y_{\text{IES}}$ | generalized node admittance matrix of IES |
| Symbols of IES-ECSR | $\psi$ | efficiency of compressor |
| | $K_\text{g}$ | pressure ratio of compressor |
| | $a_{\text{GT}}, b_{\text{GT}}, c_{\text{GT}}, d_{\text{GT}}, e_{\text{GT}}$ | heat consumption coefficients of gas generator |
| | $P_{\text{GT}}$ | active power output by the gas generator |
| | $P_{\text{GT}}^{\min}$ | lower limit of $P_{\text{GT}}$ |
| | $Y_{\text{g,pp}}, Y_{\text{g,pg}}, Y_{\text{g,gp}}, Y_{\text{g,gg}}$ | block the rearranged $Y_\text{g}$ |
| Symbols of solution and observation for ECSR | $p_{\text{n,p}}$ | node pressure vector of the constant pressure node |
| | $G_{\text{n,p}}$ | injection flow vector of the constant pressure node |
| | $p_{\text{n,g}}$ | node pressure vector of the constant injection flow node |
| | $G_{\text{n,g}}$ | injection flow vector of the constant injection flow node |

| | | | |
|---|---|---|---|
| $D^{\max}$ | Distance error threshold for hyperplane fitting | $D_i$ | The distance from the origin to the corresponding hyperplane Hi at the safety boundary |
| $H^0$ | initial hyperplane | | |
| $H_j^k$ | The hyperplane $j$ during the $k$-th segmented fitting | | |
| $D_{W_b \to H_j^k}$ | distance from $W_b$ to $H_j^k$ | | |
| $D_{W_b \to H^k}$ | The minimum value of $D_{W_b \to H_j^k}$ during the $k$-th segment fitting | | |
| $D_{W_b \to H^k}^{\max}$ | The maximum value of a corresponding to all boundary points | | |

## B. ECSR modeling results of the cases

### (1) EPS-ECSR

The EPS-ESSR of IEEE 14-node EPS is shown as equation (B1). In the equation, $Y_e$ is the node admittance matrix, $U_n$ and $I_n$ are vectors composed of node voltage and current, $K_e$ is the transformer ratio matrix.

$$\begin{cases} \boldsymbol{\Omega}_{\text{EPS-SR}} = \left\{ W_s = [S_{1,e4}\ S_{1,e5}\ S_{1,e7}\ S_{1,e9}\ S_{1,e10}\ S_{1,e11}\ S_{1,e12}\ S_{1,e13}\ S_{1,e14}]\,\middle|\,h(W_s)=0, g(W_s)\le 0 \right\} \\ s.t. \begin{cases} Y_e U_n = I_n \\ [20\ 85\ 40\ 0\ 0\ 25\ 0\ 0\ 0\ 10]^T \le [S_{1,e4}\ S_{1,e5}\ S_{1,e7}\ S_{1,e9}\ S_{1,e10}\ S_{1,e11}\ S_{1,e12}\ S_{1,e13}\ S_{1,e14}]^T \\ \le [30\ 100\ 55\ 10\ 15\ 40\ 15\ 5\ 10\ 15\ 20]^T \\ [1.06\ 1.045\ 1.01\ 0.969\ 0.97\ 1.07\ 1.012\ 1.09\ 1.006\ 1.001\ 1.007\ 1.005\ 1\ 0.986]^T \le U_n \\ \le [1.06\ 1.045\ 1.01\ 1.069\ 1.07\ 1.07\ 1.112\ 1.09\ 1.106\ 1.101\ 1.107\ 1.105\ 1\ 1.086]^T \\ [S_{be1}\ S_{be2}\ S_{be3}\ S_{be4}\ S_{be5}\ S_{be6}\ S_{be7}\ S_{be8}\ S_{be9}\ S_{be10}\ S_{be11}\ S_{be12}\ S_{be13}\ S_{be14}\ S_{be15}\ S_{be16}\ S_{be17}\ S_{be18}\ S_{be19}\ S_{be20}]^T \\ \le [200\ 100\ 100\ 75\ 50\ 50\ 75\ 50\ 25\ 75\ 25\ 25\ 25\ 25\ 50\ 10\ 25\ 10\ 5\ 10]^T \\ K_e = [0.978\quad 0.969\quad 0.932]^T \end{cases} \end{cases} \qquad \text{(B1)}$$

### (2) NGS-ECSE

The NGS-ECSR of Belgian 9-node NGS is shown as equation (B2). In the equation, $p_n$ and $G_n$ are vectors composed of node gas pressure and gas flow, $Y_g$ is the generalized node admittance matrix of the NGS [21,28]. When deriving $Y_g$, the base value of natural gas flow is introduced, which bring the main error in the linearization process of ECSR modeling. The specific derivation and base value setting process of $Y_g$ are detailed in [28].

$$\begin{cases} \boldsymbol{\Omega}_{\text{NGS-ECSR}} = \left\{ W_s = [G_{1,e3}\ G_{1,e5}\ G_{1,e8}\ G_{1,e9}]\,\middle|\,h(W_s)=0, g(W_s)\le 0 \right\} \\ s.t. \begin{cases} Y_g p_n = G_n \\ [69\ 126\ 0\ 0]^T \le [G_{1,e3}\ G_{1,e5}\ G_{1,e8}\ G_{1,e9}]^T \le [129\ 191\ 30\ 60]^T \\ [5.5\ 0\ 3\ 0\ 0\ 0\ 0\ 0\ 2.5]^T \le p_n \le [6.5\ 6.5\ 6.5\ 6.5\ 6.5\ 6.5\ 6.5\ 6.3\ 6.5\ 6.5]^T \\ [G_{bg1}\ G_{bg2}\ G_{bg3}\ G_{bg4}\ G_{bg5}\ G_{bg6}\ G_{bg7}\ G_{bg8}\ G_{bg9}\ G_{bg10}\ G_{bg11}]^T \le [231.5\ 115.7\ 231.5\ 115.7\ 231.5\ 115.7\ 231.5\ 115.7\ 115.7\ 115.7\ 115.7]^T \\ [1\ 1\ 1]^T \le K_g \le [1.2\ 1.2\ 1.2]^T \end{cases} \end{cases} \qquad \text{(B2)}$$

### (3) IES-ECSE

The NGS-ECSR of 23-node IES is shown as equation (B3). In the equation, $Y_{IES}$ is the generalized node admittance matrix of IES; $P_n$ and $F_n$ are vectors composed of node pressure (voltage or gas pressure) and flow rate (current or gas flow) respectively; $S_c$ is the power consumption of the compressor drive, $p_0$ and $T_0$ are the standard atmospheric pressure and temperature, $Z$ and $\kappa$ are the compression factor and adiabatic of natural gas, $\psi$ and $K_g$ are the efficiency and pressure ratio of compressor, $V_{GH}$ is the total calorific value of natural gas.

$$\begin{cases} \boldsymbol{\Omega}_{\text{IES-ECSR}} = \left\{ W_s = [S_{1,e4}\ S_{1,e5}\ S_{1,e7}\ S_{1,e9}\ S_{1,e10}\ S_{1,e11}\ S_{1,e12}\ S_{1,e13}\ S_{1,e14}\ G_{1,e3}\ G_{1,e5}\ G_{1,e8}\ G_{1,e9}]\,\middle|\,h(W_s)=0, g(W_s)\le 0 \right\} \\ s.t.(22-1) \begin{cases} Y_{IES} P_n = F_n \\ [1.06\ 1.045\ \cdots\ 0.986\ 5.5\ 0\ \cdots\ 2.5] \le [U_1\ U_2\ \cdots\ U_{14}\ p_1\ p_2\ \cdots\ p_9] \le [1.06\ 1.045\ \cdots\ 1.086\ 6.5\ 6.5\ \cdots\ 6.5] \\ [20\ 85\ \cdots\ 10\ 69\ 126\ 0\ 0] \le [S_{1,e4}\ S_{1,e5}\ \cdots\ S_{1,e14}\ G_{1,e3}\ G_{1,e5}\ G_{1,e8}\ G_{1,e9}] \le [30\ 100\ \cdots\ 20\ 129\ 191\ 30\ 60] \\ [S_{be1}\ S_{be2}\ \cdots\ S_{be20}\ G_{bg1}\ G_{bg2}\ \cdots\ G_{bg11}] \le [200\ 100\ \cdots\ 10\ 231.5\ 115.7\ \cdots\ 115.7] \\ [0.978\ \cdots\ 0.932\ 1\ \cdots\ 1] \le K_{IES} \le [0.978\ \cdots\ 0.932\ 1.2\ \cdots\ 1.2] \end{cases} \\ s.t.(22-2) \begin{cases} S_c = \dfrac{151.4653 p_0 Z T G_c \kappa}{\psi T_0 (\kappa-1)} (K_g^{\frac{\kappa}{\kappa-1}} - 1) \\ G_{GT} = \dfrac{1}{V_{GH}} (0.01 P_{GT}^2 + 4 P_{GT} + 150 + |15\sin(0.5(P_{GT}^{\min} - P_{GT}))|) \end{cases} \end{cases} \qquad \text{(B3)}$$